Summary

In this chapter, two cobalt based pseudopolymorphs, *viz*. [Co(2-H*ampz*)$_2$Cl$_4$], **4** and [Co(2-*ampz*)$_4$Cl$_2$], **5** (Type IV hybrid solids), were synthesized using solvent evaporation method and characterized by SCXRD, FTIR, TGA and elemental analysis. It was observed that H-bonding and π···π interactions play a major role in the stabilization of crystal packing in both the solids. Therefore, three-dimensional Hirshfeld Surfaces and associated two-dimensional finger print plots have been performed to gain insight into these interactions. The classical electrostatic energy was found to be dominant in the crystal structures as indicated by the energy framework analysis. In addition, antibacterial potential of the solids was investigated and found to possess remarkable inhibitory activity towards various bacterial strains. Further, molecular docking studies were also performed with DNA gyrase as the target protein; the synthesized complexes, particularly solid **5** exhibited good binding affinity.

III.1 Introduction

Pseudopolymorphs are solids having same chemical entities but in varying stoichiometries for example {Cu(*pdz*)Cl_2} and {Cu(*pdz*)Cl}, wherein *pdz*: pyridazine [1,2]. As discussed in chapter II, subtle changes in the synthetic parameters influence the self-assembly process which may result in the formation of new phases. While investigating the role of reaction parameters that affect the self-assembly process in the formation of polyoxomolybdate hybrid solids, a heterocyclic ligand 2-aminopyrazine (2-*ampz*) was chosen as the organic precursor instead of pyrazole (pz) as discussed in Scheme II.1. It resulted in the crystallization of pseudopolymorphs *viz.* [Co(2-H*ampz*)$_2$$Cl_4$], **4** and [Co(2-*ampz*)$_4$$Cl_2$], **5**. Both **4** and **5**, belong to Type IV of hybrid solids i.e., metal complexes.

Coordination complexes, especially transition metal complexes, are well-known for exhibiting a variety of coordination numbers, geometries, oxidation states and ligand binding affinities [3,4]. They constitute an important class of hybrid solids owing to their versatile applications in the field of catalysis, photochemistry and pharmaceuticals [5,6]. In recent years, the use of transition metal complexes as therapeutic compounds has gained great significance; particularly, cobalt based bioactive solids have been explored extensively owing to their potential as antiviral, antibacterial and anti-inflammatory agents [7-12]. Selection of ligands used for the formation of transition metal complexes is also crucial. The synergetic effect of metal centers and ligands can enhance the activity of the complexes. For instance, pyrazine and its derivatives, especially aminopyrazines, form an important group of nitrogen containing heterocyclic compounds with antibacterial, antifungal, anti-inflammatory, anti-cancer and antioxidant activities [13-15].

Therefore, the work presented in this chapter is focused on the synthesis, characterization, crystal structure, Hirshfeld surface analysis and antibacterial studies of two cobalt based pseudopolymorphs with 2-*ampz viz.* [Co(2-H*ampz*)$_2$Cl$_4$], **4** and [Co(2-*ampz*)$_4$Cl$_2$], **5**. Molecular docking studies predict the biological activities of the compounds. Hence, the potential binding interactions between the synthesized solids and selected proteins were also investigated by molecular docking studies.

III.2 Experimental

III.2.1 Synthesis

Solids **4** and **5** were synthesized using solvent evaporation technique at room temperature. **4** was synthesized using similar a synthetic protocol as described in Section II.2.1 of Chapter **2**, using 2-aminopyrazine as ligand instead of pyrazole. The purple block like crystals of **4** were obtained after 4-5 weeks in 80% yield (based on Co). **5** was crystallized from Solution **B** consisting of $CoCl_2.2H_2O$ and 2-aminopyrazine in water/methanol in 82% yield (based on Co) as shown in Scheme III.1.

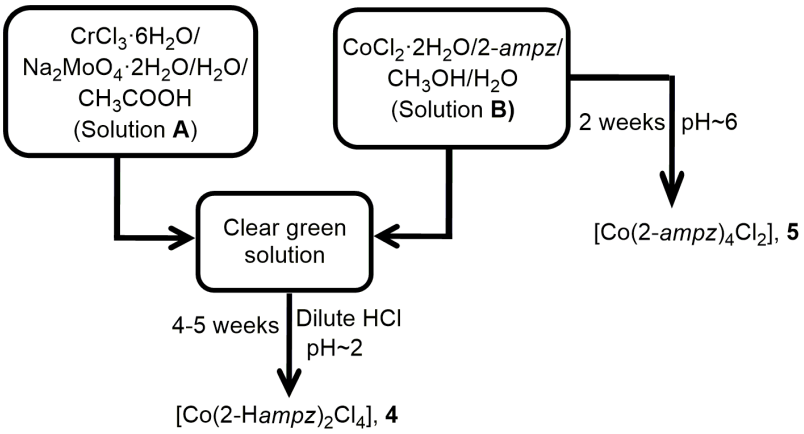

Scheme III.1 Scheme showing the synthetic pathway for the crystallization of **4** and **5**.

III.2.2 Characterization

The solids were characterized using single crystal X-ray diffraction, powder X-ray diffraction, fourier transform infrared spectroscopy and thermogravimetric analysis as discussed under Section II.2.3 in Chapter II. Crystal and refinement data have been summarized in Table III.1. Elemental analyses (C, H and N) were performed on ELEMENTAR Vario EL III CHNS Analyzer. Elem. Anal. Calcd. for **4**: C, 24.43; H, 3.05; N, 21.38. Found: C, 24.40; H, 3.03; N, 21.36%. For **5:** Calcd: C, 37.62; H, 3.91; N, 32.92. Found: C, 37.63; H, 3.92; N, 32.90%.

III.2.3 Magnetic susceptibility measurements

The magnetic susceptibilities of the solids were determined at room temperature using Guoy Balance (Sherwood, UK).

The magnetic moment and molar susceptibility are given by the following equations:

$$\text{Magnetic moment } (\mu) = 2.828 \sqrt{\chi_m} \times T$$

$$\chi_m = \chi_g \times \text{molecular weight}$$

$$\chi_g = \frac{C \times L \times (R-R_o)}{w \times 10^9}$$

where, C = Calibration constant

L = length of sample

W = weight of sample

R = sample reading

R_o = Empty tube reading

Table III.1 Crystal data and structure refinement parameters for **4** and **5**.

	4	**5**
Chemical formula	$C_8H_{12}Cl_4CoN_6$	$C_{16}H_{20}Cl_2CoN_{12}$
Molecular weight	392.97	510.27
Temperature (K)	296(2)	293(2)
Crystal system	Triclinic	Orthorhombic
Space Group	*P*-1	*P*ccn
a (Å)	7.1986(5)	7.6347(2)
b (Å)	7.3917(5)	15.7341(4)
c (Å)	7.8896(6)	18.6074(4)
α (°)	115.758(3)	90.00
β (°)	110.450(3)	90.00
γ (°)	96.904(3)	90.00
Volume ($Å^3$)	335.35(4)	2235.22(9)
Z	1	4
ρcalc ($g \cdot cm^{-3}$)	1.946	1.516
μ (mm^{-1})	2.069	1.038
F (000)	197	1044
Crystal size (mm)	0.42 x 0.35 x 0.23	0.30x 0.20x 0.15
Radiation	Mo Kα	Mo Kα
2Θ range for data collection (°)	6.362 to 56.534	3.2 to 27.5
Index ranges	$-9 \leq h \leq 9$, $-8 \leq k \leq 9$, $-10 \leq l \leq 10$	$-9 \leq h \leq 9$, $-20 \leq k \leq 20$, $-24 \leq l \leq 24$
Reflections collected	2582	2234
Independent reflections	1543 [Rint =0.0125]	2553[R_{int} = 0.024]
Data/restraints/parameters	1543/3/100	2553/4/157
Goodness-of-fit on F^2	0.899	1.057
$R[F^2 > 2\sigma(F^2)]$, $wR(F^2)$	0.0184, 0.0503	0.0250, 0.074

III.2.4 Hirshfeld surface analysis

Hirshfeld surface analysis represents a novel approach for visualization of molecular surfaces and for investigating intermolecular interactions in crystals. The Hirshfeld surface can be defined as the space occupied by a molecule in a crystal by partitioning the crystal electron density into molecular fragments and were named after F.L. Hirshfeld. Developed from Hirshfeld's idea of "stockholder partitioning" scheme for defining atoms in molecules, a weight function is defined for a molecule in a crystal by Spackman and Jayatilaka,

$$(\boldsymbol{r}) = \sum_{i \in \, molecule\ A} \rho_i^{at}(\boldsymbol{r}) \,/\, \sum_{i \in \, crystal} \rho_i^{at}(\boldsymbol{r})$$

$$= \rho_{promolecule}(\boldsymbol{r}) / \rho_{procrystal}(\boldsymbol{r})$$

where the numerator is a sum over the atoms in the molecule of interest (the promolecule) and the denominator is an analogous sum over the crystal (the procrystal). wA(r) is a continuous function with $0 < wA(r) < 1$. Hence, Hirshfeld surface is the region surrounding the molecule in the crystal where $wA(r) \geq 0.5$. It is the region where the ratio of promolecule contribution to the procrystal electron density exceeds from all other molecules in the crystal [16,17].

A van der Waals surface or an outer surface of the electron density also defines a volume around a molecule. But such molecular surfaces are defined only by the molecule itself, whereas the Hirshfeld surface is defined both by the molecule and its nearest neighbors, and hence can give information about intermolecular interactions. The presence of intermolecular interactions can be explained by mapping Hirshfeld surfaces on different properties viz., d_{norm}, d_i, d_e, molecular electrostatic potentials (MEP), curvedness and shape index. These properties can be analyzed using *Crystal Explorer* 21.5 software [18].

III.2.4.1 d_{norm}, d_e and d_i

d_{norm} is the normalized contact distance, defined in terms of d_e, d_i and the vdw radii of the atoms and mapped over red (distances shorter than sum of vdw radii) through white (distances equal to the sum of vdw radii) to blue (distances longer than sum of vdw radii) regions. 'd_{norm}' can be mathematically represented as [17]:

$$d_{norm} = \frac{(d_i - r_i^{vdw})}{r_i^{vdw}} + \frac{(d_e - r_e^{vdw})}{r_e^{vdw}}$$

where, d_e is the distance from a point on the surface to the nearest nucleus outside the surface and

d_i is the distance from a point on the surface to the nearest nucleus inside the surface;

r_i^{vdw} and r_e^{vdw} are the van der Waals radii of atoms present inside and outside the 3-D Hirshfeld surface

From the d_{norm} value, one can determine the regions involved in the intermolecular interactions in the crystals. d_i and d_e surfaces are viewed as red circular spots on each conformation and also consist of blue and green colored regions conveying the contact distances that are longer and equal to the sum of van der Waals radii. The nature of these two surfaces is also complementary to each other.

III.2.4.2 Shape index

Shape index is another interesting property of Hirshfeld surface that can represent the nature of self-complementary pairs in the crystal packing, where the two shapes differ only by a sign. Hence, it can be used to identify complementary hollows (red) and bumps (blue) where two molecular surfaces touch each other [17]. Shape index map is very sensitive to minute changes in the shape of a surface. Several small scattered yellowish-

red colored concave regions on them exhibits weak intermolecular interactions. Further, shape index also provides information on π···π interactions by the presence of red and blue colored triangular patches on surface of rings of the molecule [18,19].

III.2.4.3 Curvedness

Curvedness is a function of the root-mean-square curvature of the surface. The maps of curvedness typically show large regions of green (relatively flat) separated by dark blue edges (large positive curvature) [18]. Curvedness can be used to identify characteristic packing modes, especially planar stacking arrangements, and even the ways in which adjacent molecules contact one another. Relatively broad and flat regions on curvedness surface are characteristic of planar stacking of molecules [20]. Curvedness is a measure of ‘‘how much’’ shape, defined in terms of principal curvatures [21]. Areas on the Hirshfeld surface with a higher degree of curvedness tend to divide the surface into contact patches with each neighboring molecule; hence, the curvedness property could be used to define a coordination number in the crystal. Small yellow and red color spots may also be seen on the curvedness surface which indicates the presence of strong hydrogen bonding interactions.

III.2.4.4 Molecular electrostatic potentials (MEP)

Crystal Explorer can also generate electrostatic potential of the electron density mapped on the Hirshfeld surface. A clear insight about electrostatic interaction between neighboring molecules can be obtained which is indicated by red (electronegative) and blue (electropositive) regions on the electrostatic potential maps, while the white regions correspond to electrically neutral parts [22]. The electrostatic potentials were mapped on the Hirshfeld surface using the STO-3G basis set at the Hartree–Fock level of theory over the range ±0.1 au.

III.2.5 2-D finger print plots

2-D Finger print plot is a novel graphical method of representing the percentage contribution from various interatomic contacts in forming a 3-D Hirshfeld surface [23]. The graph is plotted using d_i and d_e distances on *x* and *y* axes respectively to represent the distance of any selected pair X and Y. These unique 'finger print' plots not only indicate which intermolecular interactions are present but also give the relative area of the surface corresponding to each kind of interaction. The contribution of each X···Y pair is represented by different colors; points with small contribution to the surface are colored blue, those with large contribution are indicated by colors ranging from green to red while the points with no contribution are left uncolored [23].

The molecular Hirshfeld surface analyses and their associated 2-D finger print plots (full and decomposed) were mapped employing the *Crystal Explorer* 21.5 program. The CIF files of the solids were given as input. The Hirshfeld surfaces were generated using a standard (high) surface resolution. The 2-D finger print plots were displayed using the expanded 0.6–2.8 Å range view with the d_i and d_e distance scales shown on the graph axes.

III.2.6 3-D Energy framework analysis

Energy frameworks provide a powerful and unique way of 3-D visualization of supramolecular aggregation of molecules in a crystal. Energy framework analysis by *Crystal Explorer* offers a better understanding of crystal packing by allowing calculation of various intermolecular interaction energies and a 3-D graphical representation of their magnitude [18]. The total interaction energy followed and used by Gavezzotti and others is [24]:

$$E_{tot} = E_{ele} + E_{pol} + E_{dis} + E_{rep}$$

which shows that the total energy framework is calculated by summing up of

E_{ele} classical electrostatic energy

E_{pol} polarization energy

E_{dis} dispersion energy

E_{rep} repulsion energy

This method was also extended to transition-metal coordination compounds as reported by Maloney *et al.* [25]. The interaction energies are calculated using molecular pair-wise interaction and are represented as cylinders joining the centroids of pairs of molecules. The radius of the cylinder is proportional to the magnitude of interaction energy.

The energy framework calculations were carried out using *Crystal Explorer* 21.5 software with HF energy model and 3-21G basis set by generating a molecular cluster around 3.8Å.

III.2.7 Antimicrobial studies

The determination of antibiotic susceptibility of a pathogen is important in selecting the most appropriate one for treating a disease. The *in vitro* screening of the antibacterial activities of the ligand, 2-aminopyrazine and its two Co(II) complexes were carried out using Kirby-Bauer Disc Method.

The Kirby-Bauer Disc Method is also called the agar diffusion method or the disk diffusion method [26]. In this method, a filter disk impregnated with an antibiotic is applied to the surface of an agar plate containing the organism to be tested and the plate is incubated at 37°C for 24-48 hours. As the substance diffuses from the filter paper into the agar, the concentration decreases as a function of the square of the distance of diffusion. At some particular distance from each disk, the antibiotic is diluted to the point that it no longer inhibits microbial growth. The effectiveness of a particular antibiotic is shown by

the presence of growth-inhibition zones. These zones of inhibition (ZOIs) appear as clear areas surrounding the disk from which the substances with antimicrobial activity diffused. The diameter of the ZOI can be measured with a ruler and the results of such an experiment constitute an antibiogram. The agar diffusion method uses commercially available filter paper disks, each containing a defined concentration of a specific antibiotic. The relative effectiveness of different antibiotics provides the basis for a sensitivity spectrum of the organism.

III.2.6.1 Materials required

Sterile petriplates, Nutrient broth, MHA agar, Antibiotic discs (gentamycin), cultures of *Escherichia coli* (*E.Coli*), *Staphylococcus saprophyticus, Bacillus subtilis* and *Pseudomonas fluorescence.*

III.2.6.2 Procedure

The sterilized molten agar of bearable warmth was poured into the petridish and left to cool and solidified. A sterile swab was dipped into the broth cultures in excess moisture by pressing the swab against the side of the tube. Swab the surface of agar completely. Then the plates were turned 90 degrees and repeated swabbing. Ran the swab around the circumference of the plate and allowed the surface to dry for about 5 minutes before placing antibiotic disc on agar. Cut wells (10mm diameter and about 2 cm apart) in each of these plates using sterile cork borer. The samples were prepared by dissolving it in DMSO (1mg/ml) and added into the wells and allowed to diffuse at room temperature. Disc with DMSO but without samples were used as the control. The standard discs were placed aseptically with sterile forceps on the agar surface. Lightly touch each disc with sterile forceps to make sure that it is in good contact with agar surface. The inoculated petri dishes were incubated upside down at 35°C. After incubation for overnight, the ZOI

was measured using a ruler at the widest diameter from one edge of the zone to the other edge. The disc diameter is reported in millimeters, looked upon the standardized chart and the result is reported as sensitive (S), resistant (R) or intermediate (I).

III.2.7 Molecular docking

Molecular docking is a computational technique used in the field of computational chemistry and drug discovery to predict the binding orientation and affinity of a small molecule (ligand) to a macromolecule (receptor), usually a protein [27].

Molecular docking typically involves three main steps: preparation of the ligand and receptor structures, generation of multiple conformations of the ligand and receptor, and scoring of the resulting conformations to identify the most likely binding mode. Various algorithms and scoring functions are used to evaluate the interactions between the ligand and receptor and to predict the binding affinity of the ligand for the receptor. The goal is to identify the optimal orientation of the ligand within the receptor, which maximizes the number of favorable interactions (such as hydrogen bonding, electrostatic interactions, and van der Waals forces) and minimizes any unfavorable interactions. Molecular docking is also used to understand the mechanism of action of drugs at the molecular level.

In silico docking studies were performed using Autodock 4.2 version [28] and the images were rendered using Biovia Discovery Studio Visualizer 2018 [29]. The crystal structures of the target enzyme/protein, DNA gyrase of *E.Coli* (PDB ID: 1AJ6) and *Bacillus subtilis* (PDB ID: 4DDQ) were obtained from the RCSB protein data bank in pdb format. The 3-D structure of the ligand 2-aminopyrazine (*2-ampz*) was downloaded from PubChem (https://pubchem.ncbi.nlm.nih.gov/compound/2-Aminopyrazine) and converted to pdb format using *Open Babel* software. The CIF files of the metal complexes were also converted to pdb using *Open Babel.* Before docking, there was a pre-treatment process

for both the proteins and the ligands. The protein preparation was done by removing the native ligands and water molecules, followed by addition of missed hydrogen atoms. 2-*ampz* and its Co(II) complexes were also prepared for docking by adding hydrogen atoms and energy minimization was carried out using force field in Autodock. Grid maps were generated using Auto Grid programme. Lamarckian genetic Algorithm (LGA) was employed as docking algoritham and all the docking parameters were set to default [30]. The structure with the lowest binding free energy was chosen for the optimum docking conformation.

III.3 Results and Discussion

III.3.1 Crystal Structure of 4 and 5

III.3.1.1 Crystal Structure of [Co(2-H*ampz*)$_2$Cl$_4$], 4

Crystal structure analysis of **4** showed that [Co(2-H*ampz*)$_2$Cl$_4$] is centro-symmetric with the metal atom at the centre of an octahedron formed by four chlorine atoms and a nitrogen atom from each of the two 2-H*ampz* molecules (Figure III.1). While, Co–N bond distance is 2.1822(11) Å; the Co–Cl bond distance was found to be 2.4583(4) and 2.4645(4) Å. Each [Co(2-H*ampz*)$_2$Cl$_4$] complex is connected to neighboring complexes through H-bonding interactions between the chloride ions and N–H groups of 2-*ampz* ligands to form 1-D chain (Table III.2). Each of these chains is connected through H-bonding interactions to two others to form a 2-D sheet (Figure III.2). Each sheet is connected to two others through π–π stacking (3.406(3) Å) between 2-H*ampz* moieties of neighboring sheets (Figure III.3). Detailed structural analysis revealed that **4** is isostructural to [Fe(2-H*ampz*)$_2$Cl$_4$] reported by Rusbridge *et. al.*[31]. Interestingly, it is also the new pseudopolymorph of [Co(2-*ampz*)$_4$Cl$_2$], **5** [32] which will be discussed in detail in Section III.3.1.2. Unlike in [Co(2-*ampz*)$_4$Cl$_2$], one of the azine nitrogen atoms in

4 is protonated. Interestingly, this protonation seems to be the key factor for the crystallization of the new pseudopolymorph [Co(2-H*ampz*)$_2$Cl$_4$].

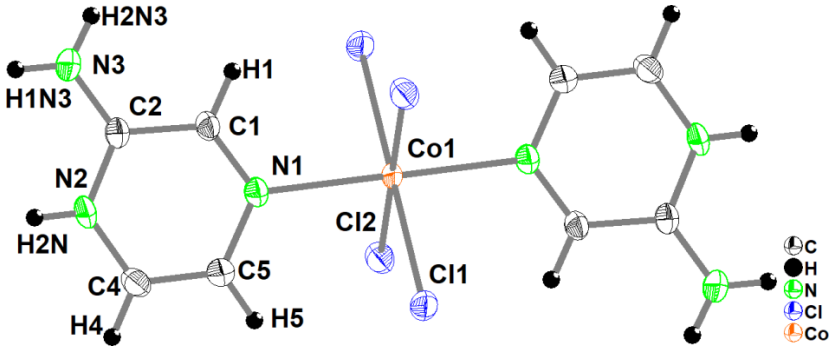

Figure III.1 ORTEP diagram of **4**. Non hydrogen atoms are shown as 50% ellipsoids and hydrogen atoms as arbitrary spheres.

Table III.2 H-bonding interactions in **4**.

D-H...A	**D-H (Å)**	**H...A (Å)**	**D...A (Å)**	**∠ D-H...A (°)**
N2-H3…Cl2	0.860(3)	2.617(4)	3.260(6)	132.52(8)
N3-H2A…Cl1	0.860(3)	2.638(4)	3.301(6)	134.82(9)
N3-H2B…Cl1	0.860(2)	2.322(5)	3.175(7)	171.65(9)

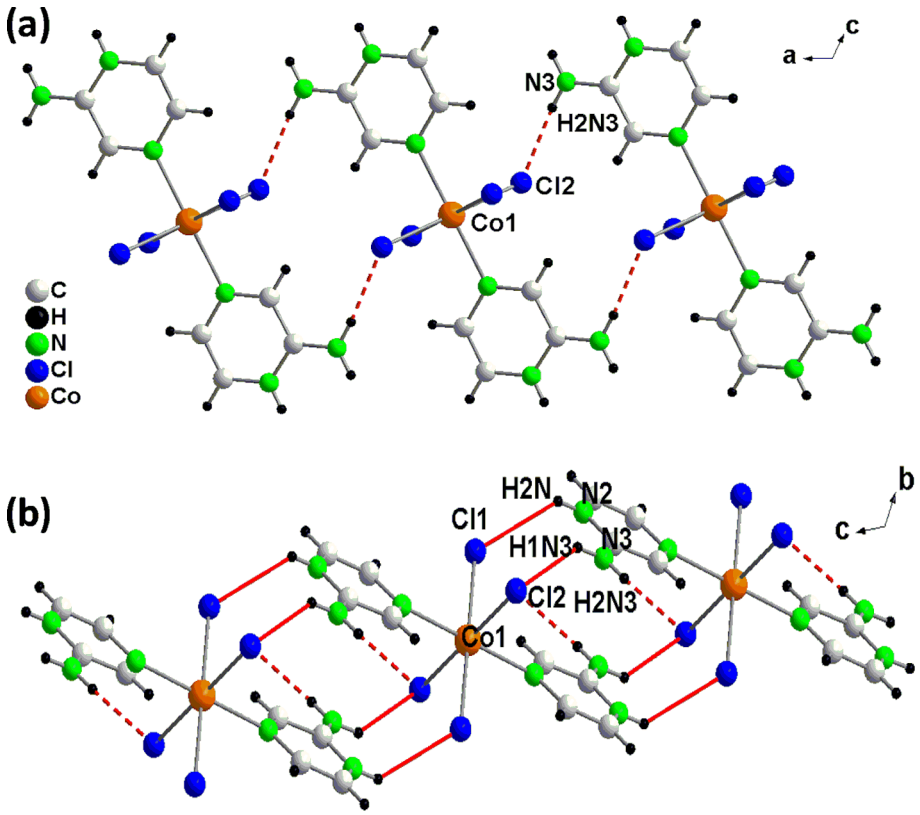

Figure III.2 (a) H···Cl interactions shown in dashed red lines link complex moieties to form 1-D chains propagating along *a* axis. (b) Inter-chain H···Cl interactions shown in solid red lines connect neighboring chains to form 2-D sheet.

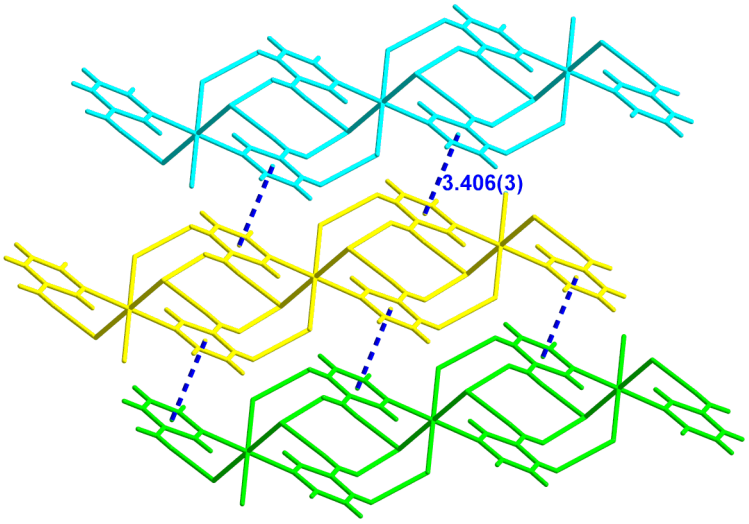

Figure III.3 Figure showing three sheets (depicted in cyan, yellow and green colors) connected to each other through π-π stacking.

III.3.1.2 Crystal structure of [Co(2-*ampz*)$_4$Cl$_2$], 5

Crystal structure of [Co(2-*ampz*)$_4$Cl$_2$] consists of Co^{2+} ion at the centre of the octahedron formed by four 2-*ampz* moieties and two chlorine atoms as shown in Figure III.4. The Co-Cl bond distance was found to be 2.421(0)Å, whereas the Co-N1 and Co-N4 bond distances being 2.207(1)Å and 2.194(1)Å respectively. Adjacent [Co(2-*ampz*)$_4$Cl$_2$] units are connected by N-H···Cl hydrogen bonding interactions of 2-*ampz* ligands to form 1-D zig-zag chains (Figure III.5a). Details of H-bonding interactions are given in Table III.3. Each 1-D chains are further connected to form 2-D sheets as shown in Figure III.5b. Intermolecular H-bonding interactions further connect the sheets to form 3-D network (Figure III.6).

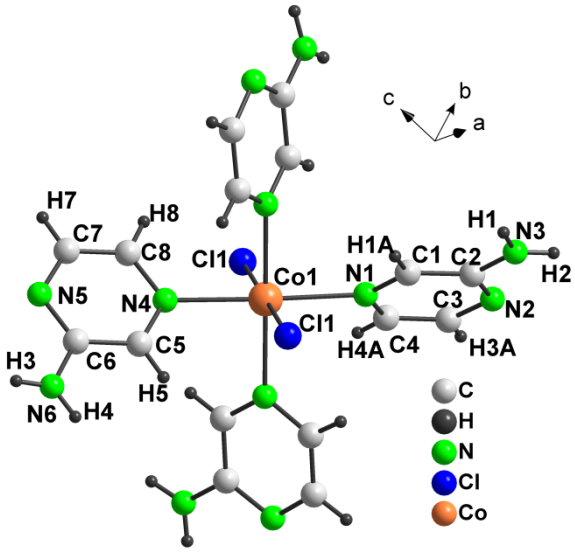

Figure III.4 Crystal structure of **5**.

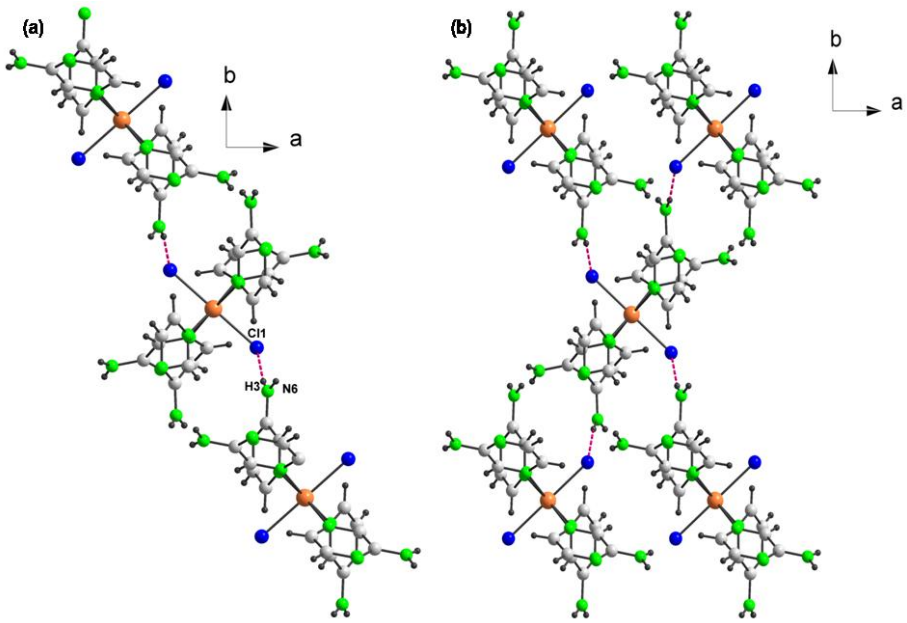

Figure III.5 (a) N-H···Cl interactions (shown in red dashed lines) leading to 1-D zig-zag chains in **5**. (b) Intermolecular H-bonding interactions connect neighboring chains to form 2-D sheets.

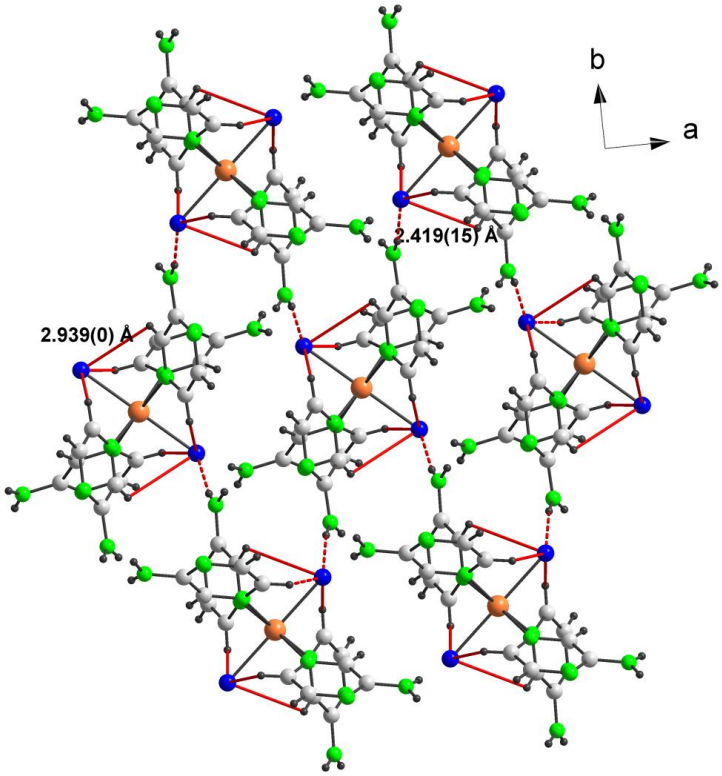

Figure III.6 Inter and intra molecular H-bonding further connects the sheets to form 3-D network. Intramolecular H-bonding is shown in solid red lines.

Table III.3 H-bonding interactions in **5**.

D-H...A	**D-H (Å)**	**H...A (Å)**	**D...A (Å)**	**∠ D-H...A (°)**
N3—H1···Cl1	0.85 (1)	2.36 (1)	3.209 (2)	175 (2)
N3—H2···N5	0.86 (1)	2.43 (2)	3.134 (2)	140 (2)
N6—H3···Cl1	0.85 (1)	2.42 (1)	3.265 (1)	171 (2)
N6—H4···N2	0.86 (1)	2.33 (2)	3.045 (2)	142 (2)

III.3.2 Vibrational and Thermal analyses

The FTIR spectra of **4** and **5** (Figure III.7) displayed bands in the region 3300-300 cm^{-1} due to N-H stretching vibrations of the 2-aminopyrazine ligand. The strong peaks in the range 1650- 1530 cm^{-1} could be attributed to N-H bending vibrations. A medium intensity band due to the C-N stretching was observed at around 1200 cm^{-1}. The low frequency region of the spectra indicated the presence of a medium intensity band at around 420 cm^{-1} in **4** and 428 cm^{-1} in **5** due to Co-Cl vibrations.

Figure III.8 shows the TG plots of **4** and **5**. TG analysis of **4** showed weight loss in two steps; an initial weight loss of 49.2% upto 360°C corresponding to the loss of two 2-*ampz* moieties (calcd. 48.3%). The second weight loss of 37.4% upto 690°C was observed in **4** corresponding to the loss of four chloride units (calcd. 36.1%). The residual 13.4% could be attributed to cobalt metal. On the other hand, in **5**, the first weight loss upto 370°C corresponding to 75% was due to the degradation of four 2-*ampz* moieties (calcd. 74.5%). Subsequent weight loss of 14% upto 700°C could be assigned to the loss of two chloride units (calcd. 13.9%). The remaining 11% could be attributed to cobalt metal.

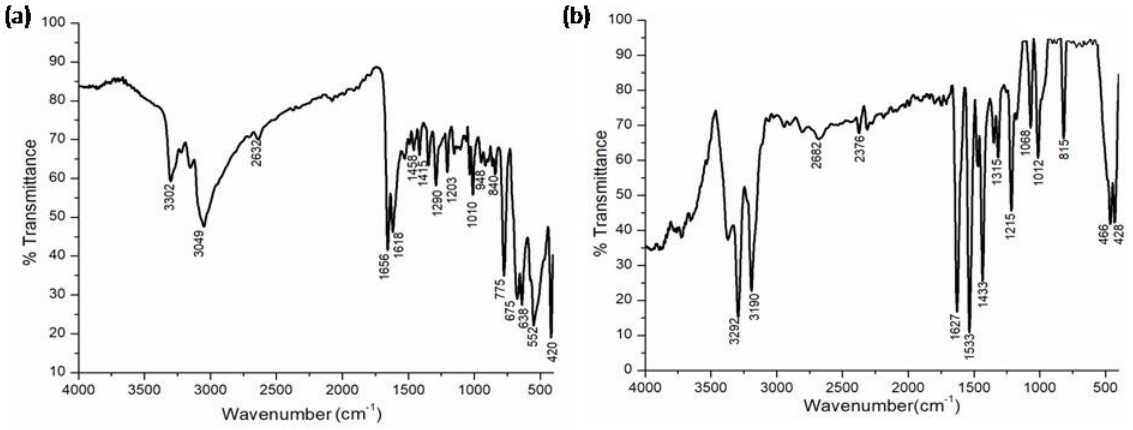

Figure III.7 FTIR spectrum of (a) **4** and (b) **5**.

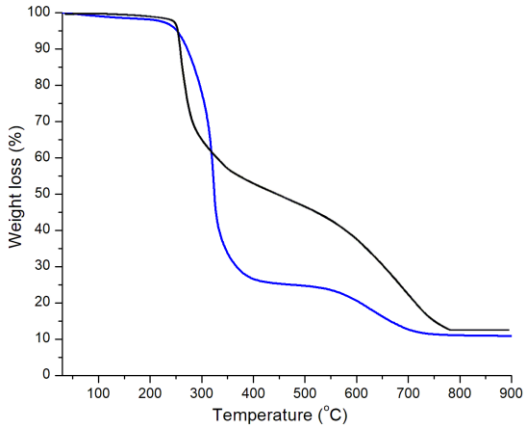

Figure III.8 TG plots of **4** (black) and **5** (blue).

III.3.3 Hirshfeld surface analyses

The Hirshfeld surface of **4** cover 309.80 Å^2 area and spread over 328.40 Å^3 volumes with 0.5 isovalue. The 3-D "d_{norm}" surfaces were mapped (along *c* axis) over a fixed color scale of -0.484 to 0.949 Å, d_i ranging from 0.790 to 2.397 Å, d_e in the color scale of 0.790 to 2.398 Å, whereas, shape index mapped within the color range of -1.000 to 1.000 Å, and curvedness in the range of -4.000 to 0.400 Å respectively (along *b* axis), as shown in Figure III.9. The surfaces are shown transparent to permit visualization of the crystal structure.

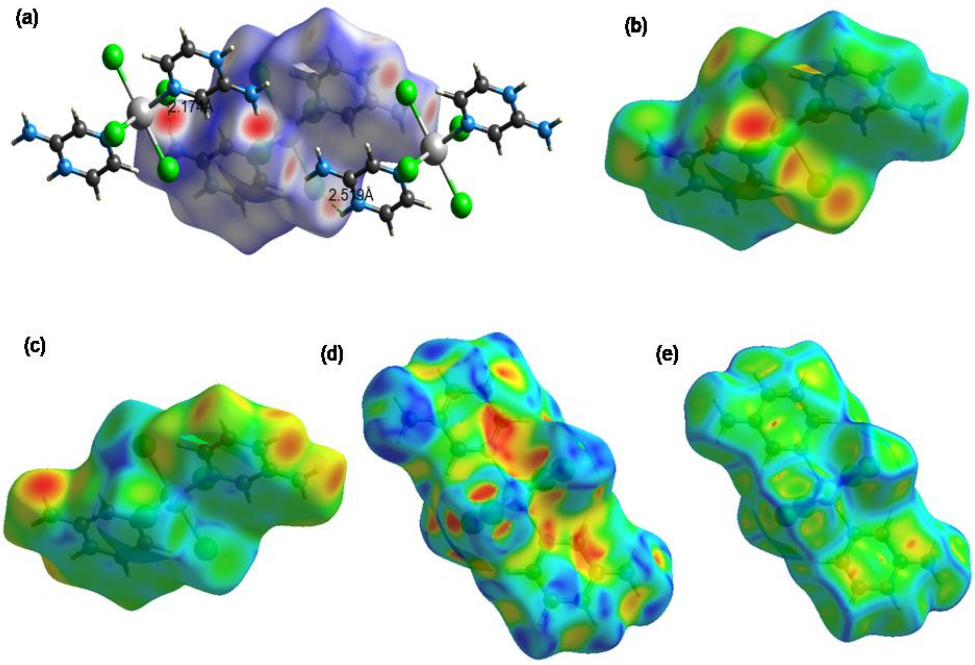

Figure III.9 Hirshfeld surfaces for visualizing the intermolecular contacts in **4** (a) d_{norm} highlighting the regions of N—H···Cl hydrogen bonds, (b) d_e, (c) d_i, (d) shape index and (e) curvedness.

The red spots inside the contours on shape index map indicate intermolecular interactions as given in Table III.3. The appearance of consecutive red and blue triangular patches over the aromatic ring in the shape index map (Figure III.9d) confirms the presence of weak π···π interactions in the crystal packing.

The large flat regions delineated by a blue outline on the curvedness map (Figure III.9e) shows the planar stacking of molecules [17].

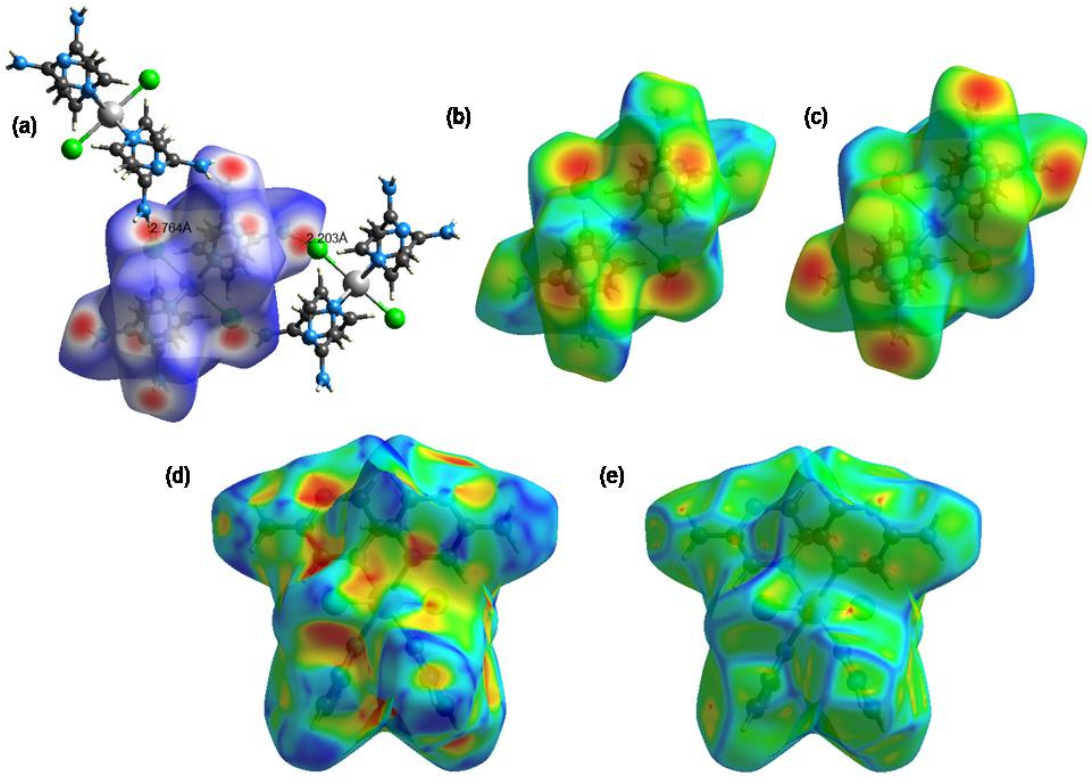

Figure III.10 Hirshfeld surfaces for visualizing the intermolecular contacts in **5** (a) dnorm highlighting the regions of N—H···Cl hydrogen bonds, (b) d_e, (c) d_i, (d) shape index and (e) curvedness (along *b* axis).

The Hirshfeld surface of **5** spread over 444.03 Å^2 area and holds 548.96 Å^3 volume with 0.5 isovalue; the scaled color patches on the surface were generated in the range -0.454 to 1.180Å, 0.810 to 2.660Å, 0.811 to 2.610 Å for d_{norm}, d_i and d_e respectively, whereas the shape index plot and curvedness plot are engendered from -1.00 to 1.00 a.u. and -4.000 to 0.400 a.u., respectively, as shown in Figure III.10. As discussed in the Hirshfeld surface (HS) of **4**, red circular spots on the Hirshfeld surface of **5** indicate intermolecular close contacts of N-H···Cl hydrogen bonding interactions as shown in Figure III.10a. Shape index map and curvedness map shows the characteristic features of weak π···π stacking interactions in the crystal structure of **5** (Figures III.10d and 10e).

III.3.3.1 Molecular electrostatic potentials (MEP)

The electrostatic potential maps reveal the electropositive regions represented by blue color and electronegative regions represented by red color in the molecules as shown in Figure III.11. In **4,** red color regions can be seen near the chlorine atoms corresponding to highly electrostatic negative acceptor potential whereas in **5** electronegative spots indicated by red color can be seen around chlorine atoms and also nitrogen atoms in the aromatic ring.

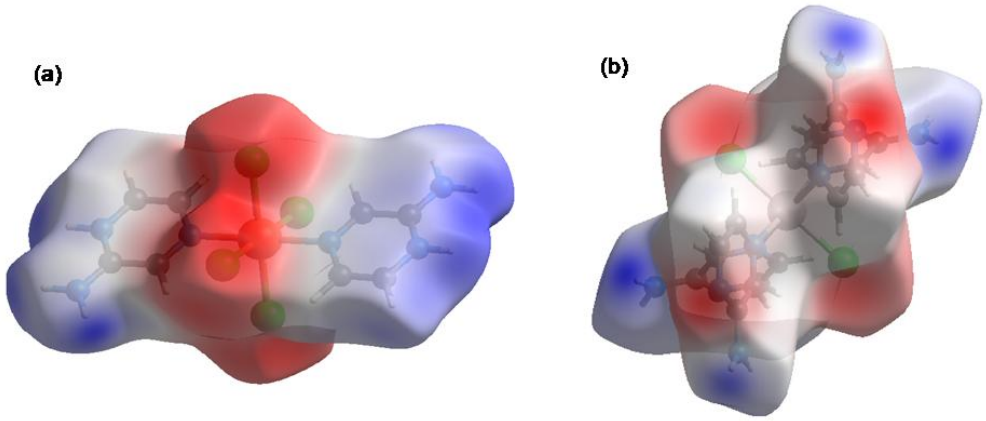

Figure III.11 Electrostatic potential mapped on the Hirshfeld surface of (a) **4** and (b) **5**.

III.3.3.2 Finger print plots

The 2-D finger print plots for overall and individual interactions in the crystal packing of solids **4** and **5** were calculated and results are shown in Figures III.12 and III.13 respectively.

In **4,** the major contribution to the HS area is due to H···Cl/Cl···H contacts (51.2%). H···Cl/Cl···H contacts can be attributed to N-H···Cl hydrogen bonding interactions and appear as two sharp symmetric spikes in the finger print plots of **4** (refer Figure III.12b). The second major contact is H···H, since it has a contribution of 22% to the total surface area (Figure III.12c). The C···H, N···H contacts also have significant contributions to the HS in **4** as can be seen in the 2-D plots.

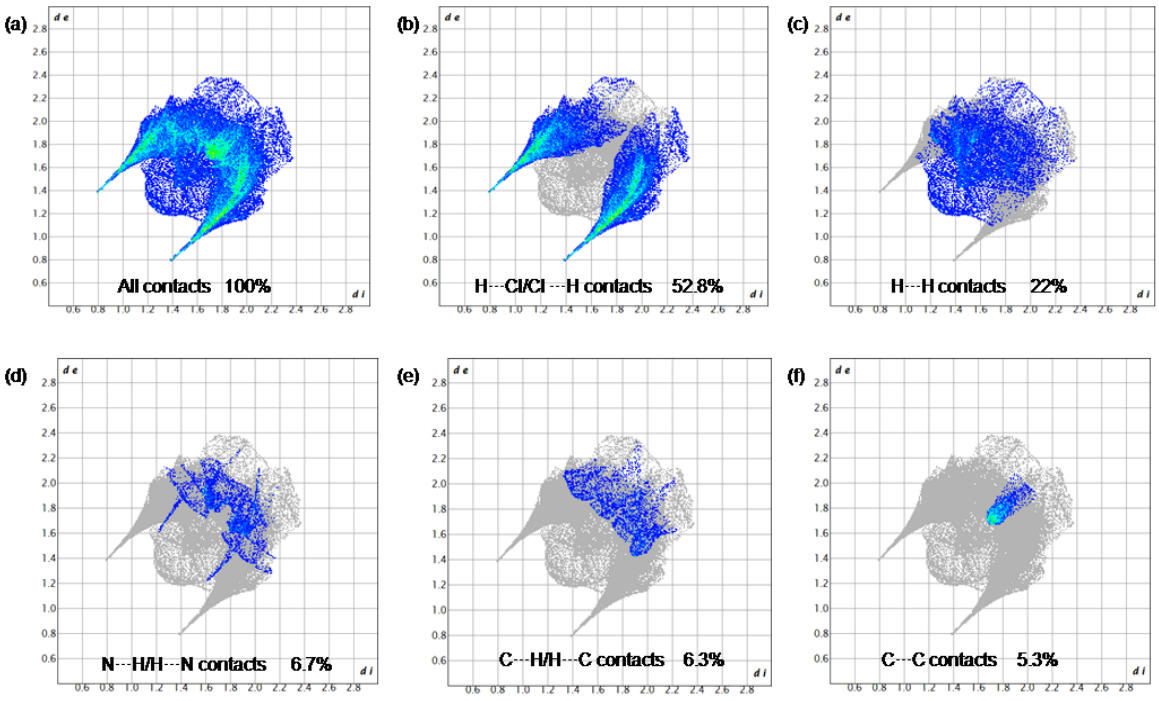

Figure III.12 2-D finger print plots of solid **4** showing the contributions of different types of interactions: (a) all intermolecular contacts, (b) H···Cl/Cl···H contacts, (c) H···H contacts, (d) N···H/H···N contacts, (e) C···H/H···C contacts and (f) C···C contacts. The outline of the full finger print is shown in grey.

Finger print plots revealed that H···Cl interactions plays a major role in the stabilization of crystal packing in **4**. However, in **5**, the H···H interactions are the most abundant contributing to 42.9% to the total Hirshfeld surface area as shown in Figure III.13b, followed by N···H interactions (23.8%) characterized by two sharp symmetric spikes at d_e+d_i~2.6Å (Figure III.13d). This is due to the abundance of H and N on the molecular surface of solid **5** arising from four 2-aminopyrazine moieties in the unit cell. H···Cl interactions also contribute significantly (15.7%) to the HS appearing as two prominent long spikes at d_e+d_i~2.8Å as shown in Figure III.13c. In addition, as can be seen in Figure III.13e, the C···H contacts contribute 12.9% to the Hirshfeld surface characterized by two symmetric wings in the FP plot.

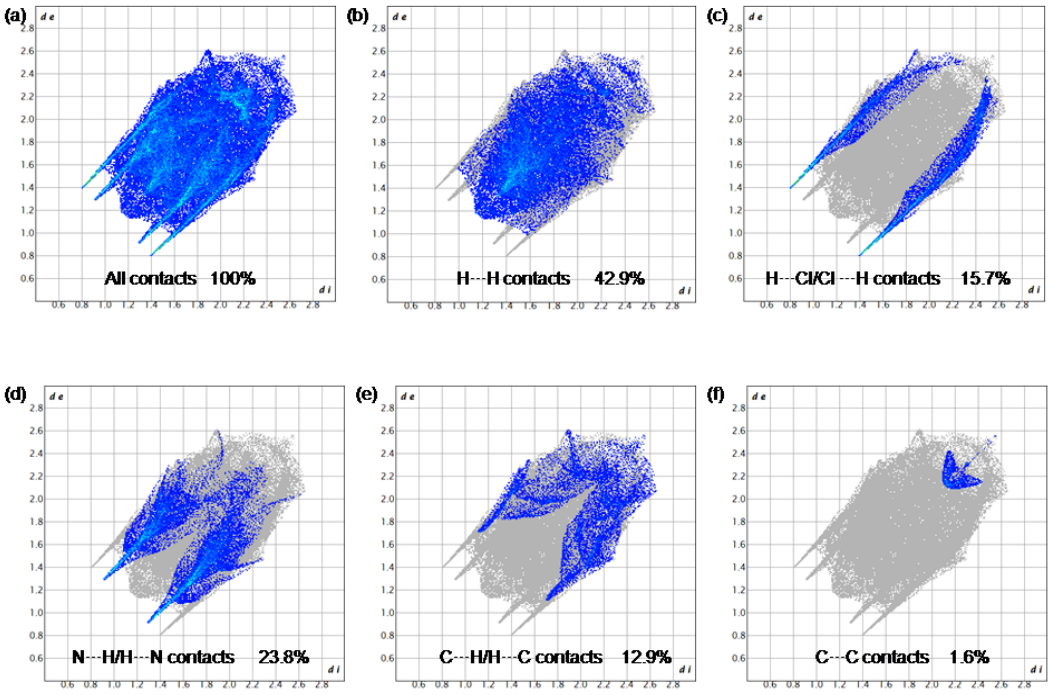

Figure III.13 2-D finger print plots of solid **5** showing the contributions of different types of interactions: (a) all intermolecular contacts, (b) H···H contacts, (c) H···Cl/Cl···H contacts, (d) N···H/H···N contacts, (e) C···H/H···C contacts and (f) C···C contacts. The outline of the full finger print is shown in grey.

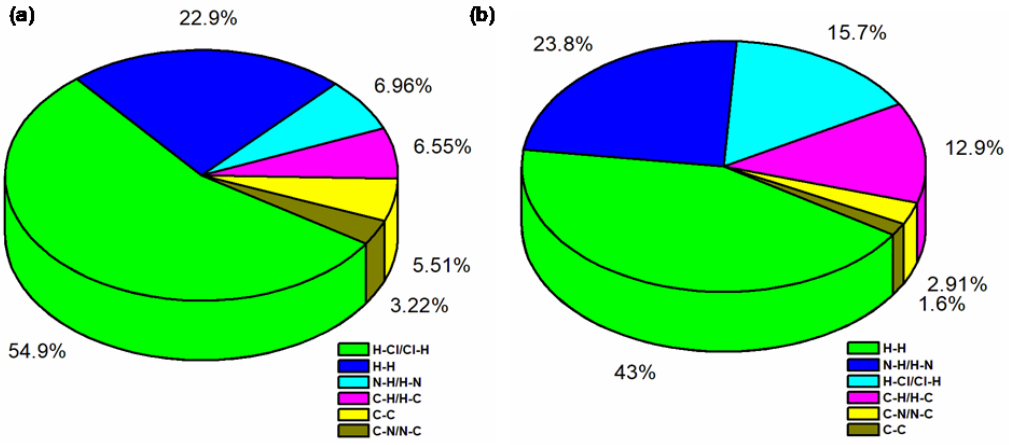

Figure III.14 Graphical representation of the contribution of interatomic contacts in the crystal packing of (a) **4** and (b) **5**.

III.3.4 Energy framework analysis

The various intermolecular interaction energies were computed for solids **4** and **5** by 3-D energy frameworks using the default red, green and blue colored solid cylinders in the construction of Columbic or classical electrostatic E_{ele}, dispersion E_{dis} and total energy components E_{tot}, respectively. The molecular pairs involved in the calculation of interaction energies for **4** and **5** are shown in Figures III.15.

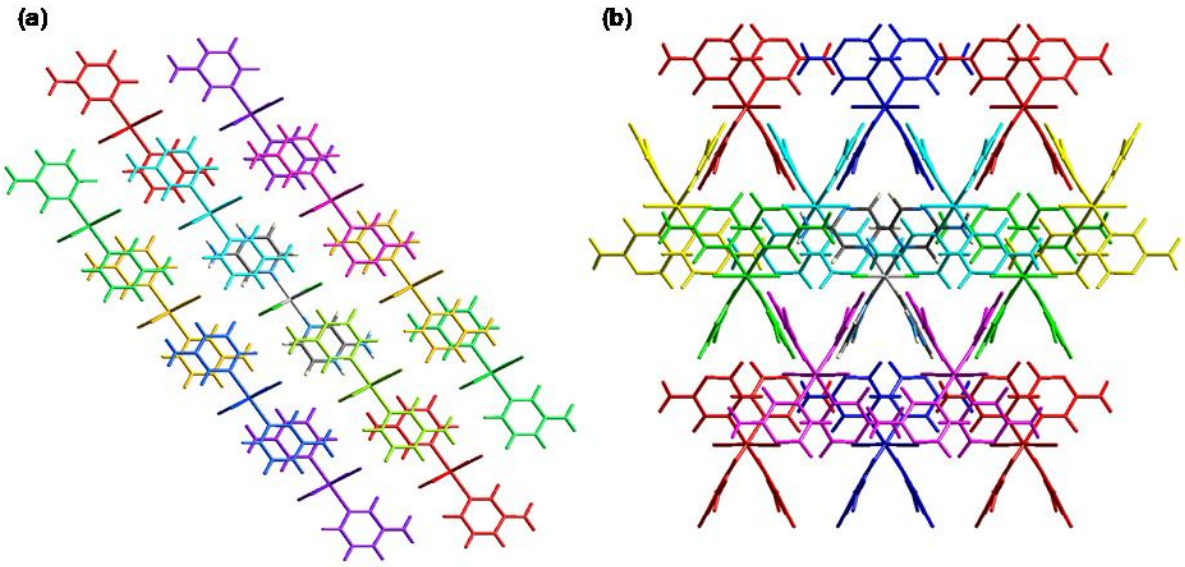

Figure III.15 Molecular pairs involved in the interaction of (a) **4** and (b) **5**.

3-D energy frameworks corresponding to coulomb energy (red), dispersion energy (green) and total energy (blue) along the crystallographic axis is displayed in Figures III.16 and III.17 for solids **4** and **5** respectively.

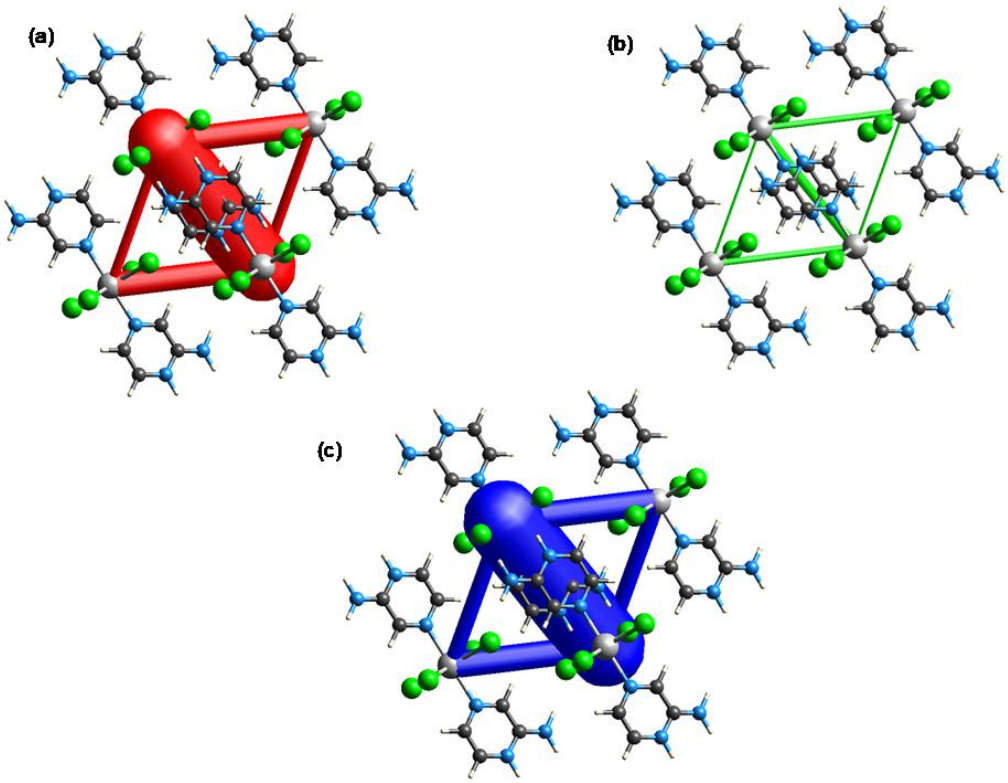

Figure III.16 Energy framework diagrams for a cluster of molecules in **4:** (a) electrostatic or Coulomb energy, E_{ele}; (b) dispersion energy, E_{dis} **(c)** total energy, E_{tot}. The cylindrical radius was adjusted to the scale factor of 80 kJ mol^{-1} with a cut-off value of 10 kJ mol^{-1}. Weak molecular interactions below threshold energy value of 10 kJ mol^{-1} were omitted for clarity.

As discussed in section III.2.6, the thickness of the cylinders in each energy framework corresponds to the strength of the interaction energies between respective molecular pairs which were also confirmed by the higher negative energy values as shown in Tables III.4 and III.5. The tables provide information on various interaction energies and total energies based on a color code scheme of molecular pairs interacting. In addition, other information can be obtained from the table, such as the existence of rotational symmetry operations with respect to the reference molecule (*Symop*), the centroid-to-centroid

distance in Å between the reference molecule and interacting molecules (*R*) and the number of pair(s) of interacting molecules with respect to the reference molecule (*N*), which helps in the calculation of lattice energy of a crystal [33].

Table III.4 Interaction Energies (kJ/mol) in component form of **4**.

$$\mathbf{E_{tot} = E_{ele} \times k_{ele} + E_{pol} \times k_{pol} + E_{dis} \times k_{dis} + E_{rep} \times k_{rep}}$$

Color code	N	Symop	R	Electron Density	E_{ele}	E_{pol}	E_{dis}	E_{rep}	E_{tot}
	2	x, y, z	15.01	HF/3-21G	0.0	-7.3	0.0	0.0	-4.7
	2	x, y, z	7.20	HF/3-21G	-114.4	-90.0	-35.2	103.6	-122.7
	2	x, y, z	8.10	HF/3-21G	-326.9	-117.3	-66.8	96.5	-391.4
	2	x, y, z	13.79	HF/3-21G	0.0	-3.5	0.0	0.0	-2.2
	2	x, y, z	8.62	HF/3-21G	-317.3	-112.8	-56.7	94.7	-371.0
	2	x, y, z	8.14	HF/3-21G	-40.9	-30.7	-16.7	23.4	-57.8
	2	x, y, z	12.72	HF/3-21G	0.0	-6.9	0.0	0.0	-4.5
	2	x, y, z	7.89	HF/3-21G	-47.5	-35.6	-15.1	14.0	-73.8

Scale factors for benchmarked energy models

Energy Model	k_{ele}	k_{pol}	k_{disp}	k_{rep}
CE-HF ... HF/3-21G electron densities	1.019	0.651	0.901	0.811
CE-B3LYP ... B3LYP/6-31G(d,p) electron densities	1.057	0.740	0.871	0.618

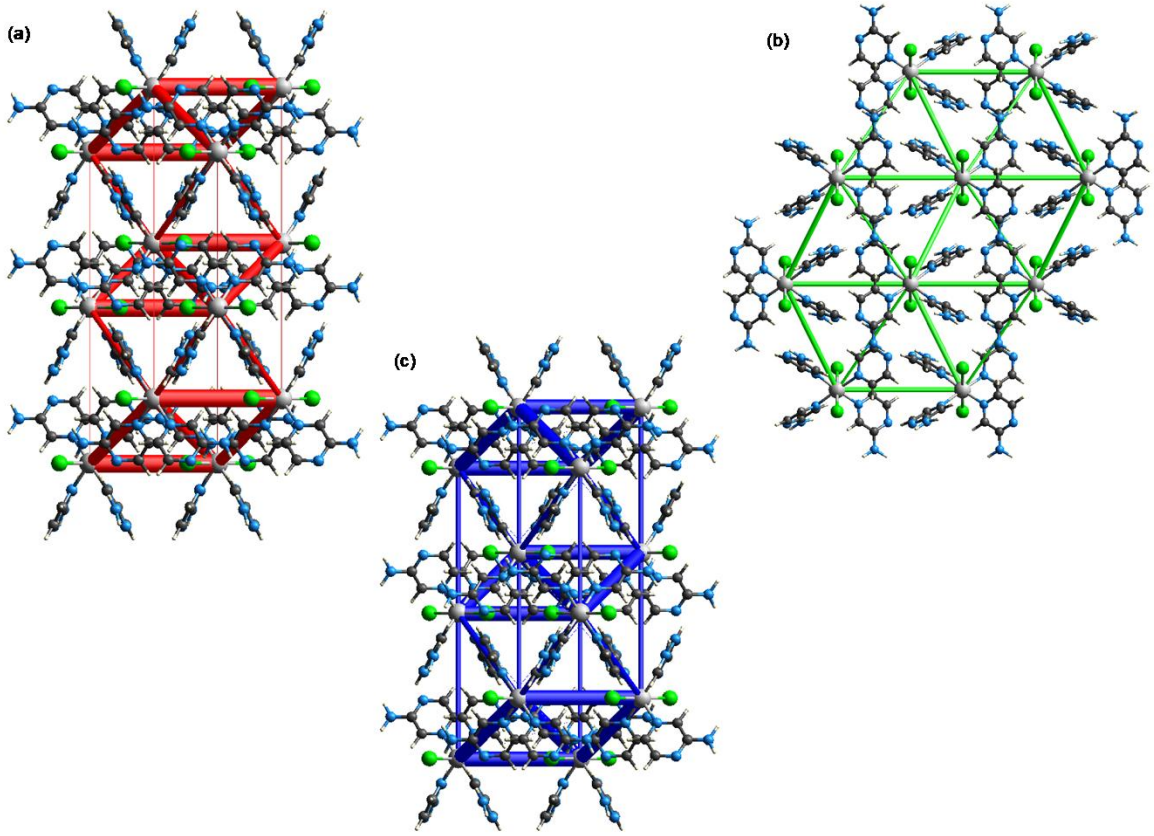

Figure III.17 Energy framework diagrams for a cluster of molecules in **5**: (a) electrostatic or Coulomb energy, E_{ele}; (b) dispersion energy, E_{dis} **(c)** total energy, E_{tot}. The cylindrical radius was adjusted to the scale factor of 80 kJ mol^{-1} with a cut-off value of 10 kJ mol^{-1}. Weak molecular interactions below threshold energy value of 10 kJ mol^{-1} were omitted for clarity.

$k_{el}e$, k_{dis}, k_{pol} and k_{rep} are the conversion factors for calculation of total energies which are reported only for two benchmarked energy models of electron density functions CE-HF…HF/3-21G and CE-B3LYP…B3LYP/6-31G(d,p), scaled appropriately and are displayed just below the tables III.4 and III.5 [34].

Table III.5 Interaction Energies (kJ/mol) in component form of **5.**

Color code	N	Symop	R	Electron Density	E_{ele}	E_{pol}	E_{dis}	E_{rep}	E_{tot}
	4	-x+1/2, y, z+1/2	12.04	HF/3-21G	0.0	-3.7	0.0	0.0	-2.4
	2	-x, -y, -z	14.43	HF/3-21G	0.0	-0.4	0.0	0.0	-0.2
	2	x, y, z	7.63	HF/3-21G	-104.3	-35.6	-42.5	91.6	-93.5
	2	-x, -y, -z	9.57	HF/3-21G	-70.7	-15.6	-44.1	38.4	-90.8
	2	-x+1/2, y, z+1/2	9.30	HF/3-21G	-4.5	-2.0	-39.7	13.7	-30.5
	4	x+1/2, -y, -z+1/2	10.28	HF/3-21G	-36.6	-12.8	-23.6	36.0	-37.7

Scale factors for benchmarked energy models

Energy Model	k_{ele}	k_{pol}	k_{disp}	k_{rep}
CE-HF ... HF/3-21G electron densities	1.019	0.651	0.901	0.811
CE-B3LYP ... B3LYP/6-31G(d,p) electron densities	1.057	0.740	0.871	0.618

The highest total interaction energy obtained was, E_{tot} = -391.4 kJ/mol in solid **4** at the molecular centroid distance R = 8.10Å (refer Table III.4). In **5,** the highest total interaction energy obtained was E_{tot} = -93.5kJ/mol as can be seen in table III.5.

An overall analysis of energy frameworks of **4** and **5** show that the major contribution towards the interaction energies comes from classical electrostatic or coulomb energy followed by dispersion energy. From the energy framework diagrams (Figures III.16 and III.17) and the interaction energy tables (tables III.4 and III.5), it can be inferred that classical electrostatic/Coulomb energy, E_{ele} dominates over the dispersion energy, E_{dis} frameworks in both solids **4** and **5.**

III.3.5 Antibacterial activities

Solids **4, 5**, ligand **(**2-aminopyrazine) and cobalt chloride were screened for their antibacterial activity against four different bacterial strains; two-gram positive bacteria: *Staphylococcus saprophyticus, Bacillus subtilis* and two gram negative bacteria*: E. Coli, Pseudomonas fluorescence.* Gentamycin was used as the standard. The solvent (DMSO) was used as the control. The results are shown in Figure III.18. The calculated zone of inhibition is listed in Table III.6

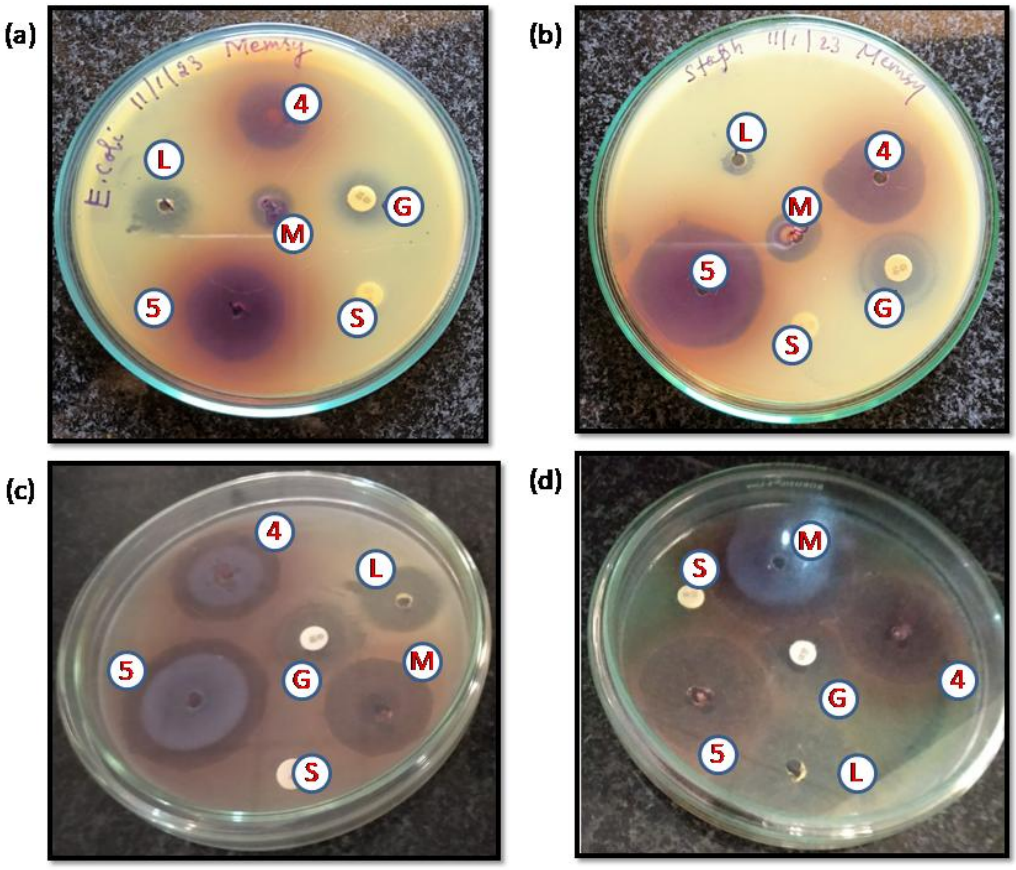

Figure III.18 Anti bacterial activity of solids **4** and **5** compared with 2-*ampz*, cobalt chloride and standard antibiotic Gentamycin (S-solvent, L-2-*ampz*, M-cobalt chloride, G-Gentamycin); (a) *Escherichia Coli*, (b) *Staphylococcus saprophyticus*, (c) *Bacillus subtilis* and (d) *Pseudomonas fluorescence.*

Table III.6 Anti bacterial activity (zone of inhibition) against clinical pathogens.

Microorganism	**Zone of inhibition (mm)**				
	4	**5**	2-*ampz*	$CoCl_2.6H_2O$	Standard (Gentamycin)
E.Coli	19	25	12	10	15
Staphylococcus saprophyticus	22	32	14	16	20
Bacillus subtilis	25	38	20	23	18
Pseudomonas fluorescence	32	36	28	26	16
Solvent-DMSO	No activity				

From the anti bacterial studies, it was observed that **4** and **5** showed higher activities than the free ligand 2-*ampz* and metal chloride, $CoCl_2.6H_2O$. Both solids showed higher activities when compared with the standard Gentamycin towards both gram-positive and gram-negative bacteria. Solid **5** was particularly more sensitive than solid **4** towards all bacterial strains. The greater sensitivity of **5** could be attributed to the presence of four 2-*ampz* moieties in the structure in contrast to two 2-*ampz* units in **4.**

The higher activity of metal complexes when compared to ligand can be explained on the basis of Tweedy's chelation theory [35,36]. Chelation reduces the polarity of the metal ion due to partial sharing of the positive charge with the donor atom of the ligand and also due to delocalization of π-electrons over the chelate ring. This decrease in the polarity enhances the lipophilic nature of the complexes, which makes it easier to penetrate the cell walls of microorganisms thus interfering with the normal cell processes.

III.3.6 Molecular docking studies

In order to better understand the antibacterial potentials of **4** and **5,** molecular docking studies were carried out using DNA gyrase present in *E.Coli* (PDB ID: 1AJ6) and *Bacillus Subtilis* (PDB ID: 4DDQ) as the protein target. The DNA gyrase enzyme, a subclass of Topoisomerase II, is an attractive target due to its presence in all microbes. It plays a significant role in DNA replication and catalyses the ATP-dependent negative super-coiling of double-stranded closed-circular DNA [37].

The negative values of the binding free energy of the docked complexes (refer Table III.7) indicated that the complexes reasonably bind to the DNA gyrase. 2-*ampz* and solids **4** and **5** interact with the target enzyme mainly through H-bonding and Vander Waals interactions.

Table III.7 Interaction of 2-*ampz*, **4** and **5** with protein targets, 1AJ6 and 4DDQ.

Compound	**1AJ6**		**4DDQ**	
	Interacting residues (H-bonding)	**B.E (kcal/mol)**	**Interacting residues (H-bonding)**	**B.E (kcal/mol)**
2-*ampz*	GLY77, ARG76, GLU50	-3.8	VAL38, ARG39	-3.59
4	VAL118, VAL97, ASN46, ASP49	-5.06	PHE479, ASP481, MET102, VAL104	-3.65
5	ALA100, ILE94, ASP45, ASN46	-5.70	ASP297, ARG298, ARG484, ASP96, PRO219, LEU264, ALA221	-6.37

The binding energies of 2-*ampz*, **4** and **5** with 1AJ6 were found to be -3.8, -5.06 and -5.70 kcal/mol respectively. With 4DDQ, binding energies were -3.59, -3.65 and -6.37 kcal/mol for 2-*ampz*, **4** and **5** respectively. In this analysis, **5** showed relatively high negative binding energies, indicating its greater affinity towards DNA gyrase. Strong H-bonding interactions could be the reason for the enhanced activity of **5** than **4**. The results were in

good agreement with the wet lab experiments. The docking results with DNA gyrase present in *E.Coli* and *Bacillus Subtilis* are represented in figures III.19 and III.20 respectively.

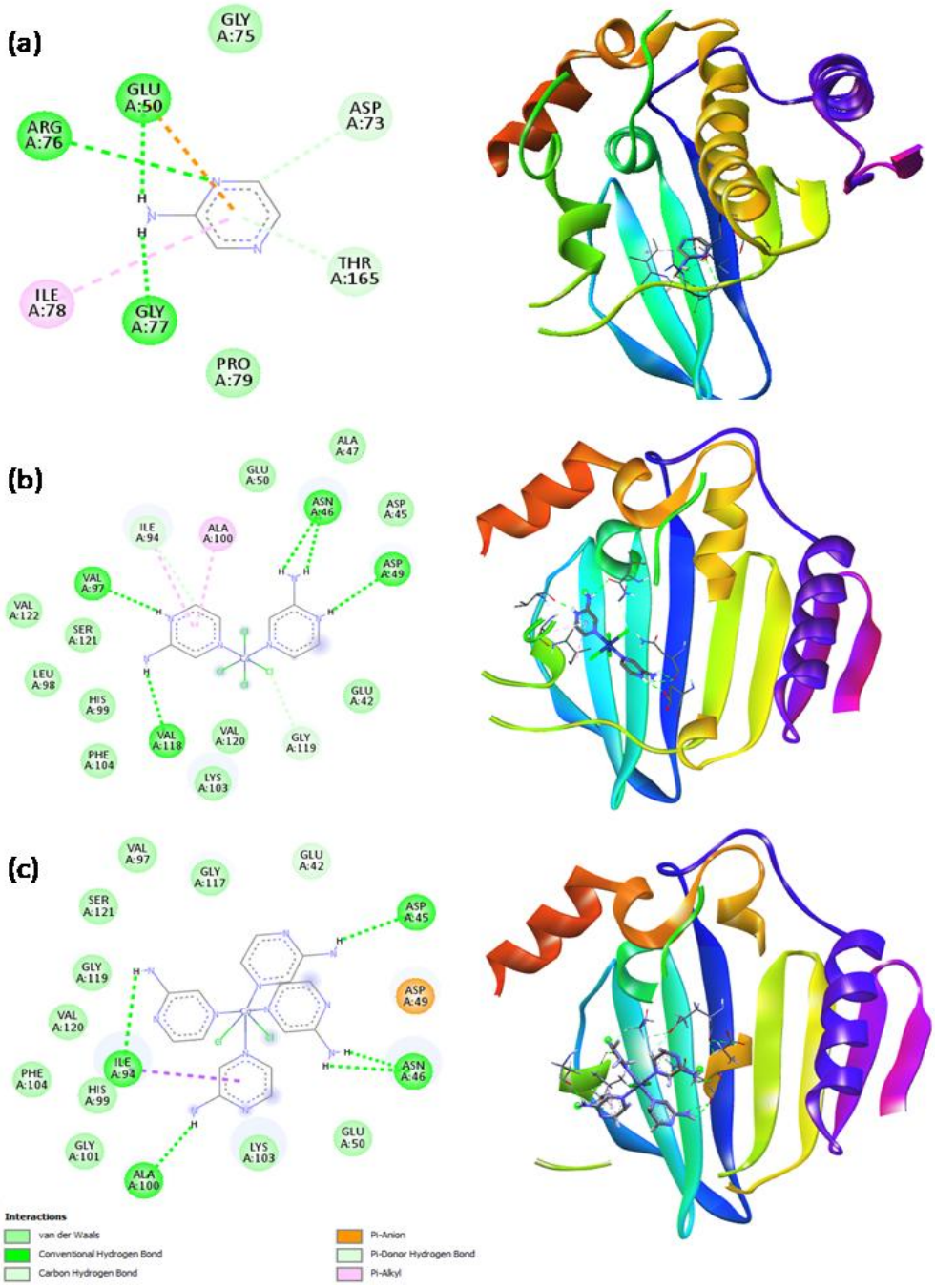

Figure III.19 Molecular docking of (a) 2-*ampz*, (b) **4** and (c) **5** with the target protein PDB ID: 1AJ6. Left and right hand images represent 2-D and 3-D interaction diagrams respectively.

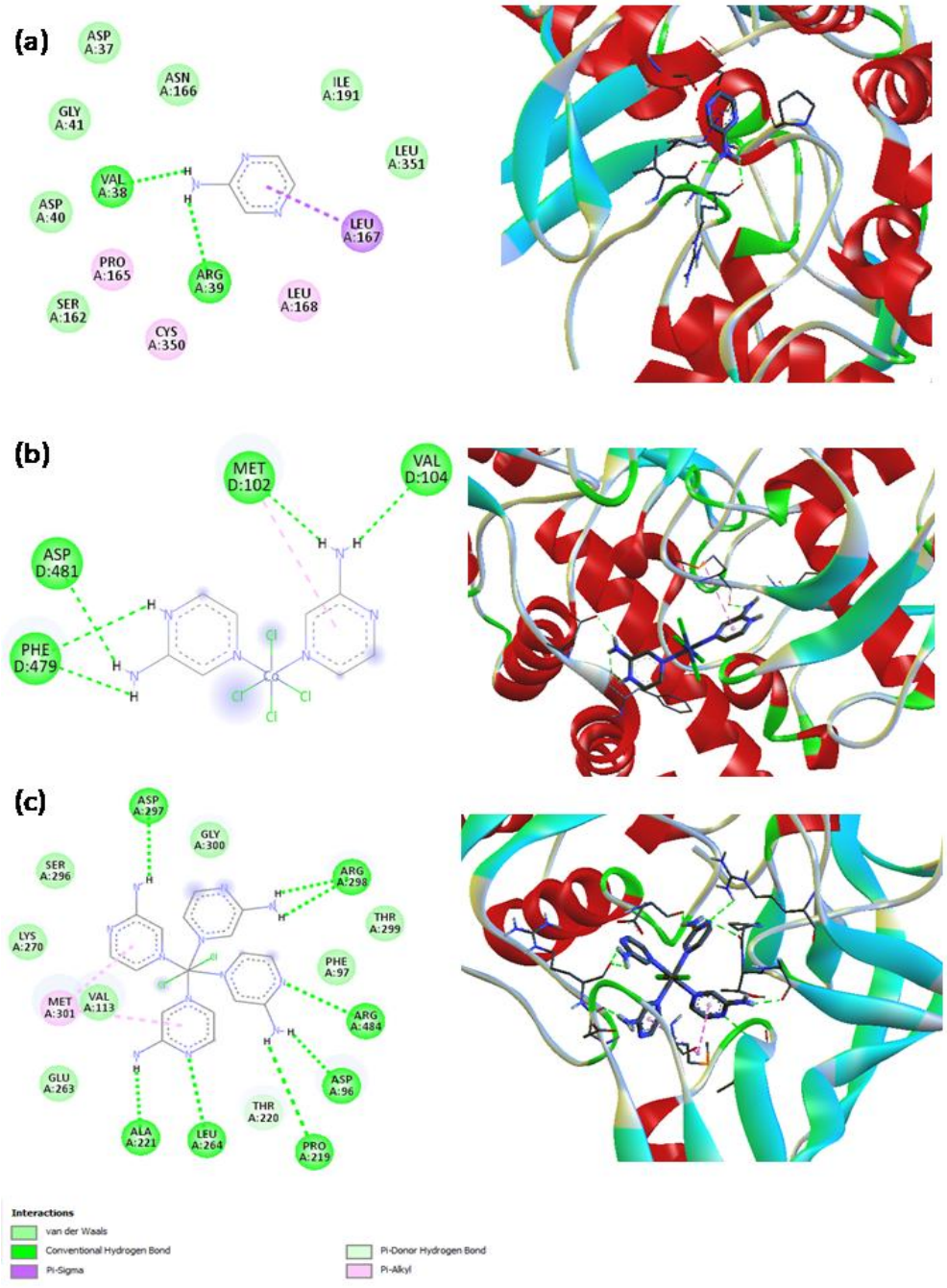

Figure III.20 Molecular docking of (a) 2-*ampz*, (b) **4** and (c) **5** with the target protein PDB ID: 4DDQ. Left and right hand images represent 2-D and 3-D interaction diagrams respectively.

III.3.8 Magnetic properties

For solids **4-5**, the magnetic moment was calculated using spin only formula, $\mu = [n(n+2)]^{1/2}$ BM (where n is number of unpaired electrons).

In solids **4-5**, only one cobalt center is present and the observed magnetic moment obtained was 4.61 and 5.83 BM respectively. The calculated magnetic moment using spin only formula is 3.80. Therefore, the observed value showed a deviation from the calculated values which indicated that other parameters seem to be affect the magnetic behavior of these two solids.

III.4 Conclusions

Two cobalt based pseudopolymorphs with 2-*ampz viz.* [Co(2-H*ampz*)$_2$Cl$_4$], **4** and [Co(2-*ampz*)$_4$Cl$_2$], **5** were synthesized using solvent evaporation method and characterized by SCXRD, FTIR, TGA and elemental analysis. The role of non-covalent interactions that stabilize the crystal packing was investigated in detail using Hirshfeld surface analyses, finger print plots and energy framework analysis. The metal complexes **4** and **5** showed significant antibacterial activities when compared with the ligand, 2-*ampz* and with the standard antibiotic Gentamycin. **5** exhibited greater sensitivity towards all bacterial strains. Molecular docking studies were carried out to substantiate the *in vitro* antibacterial studies and also to find out the best binding site of the complexes with the target protein. From the *in vitro* and *in silico* studies it can be concluded that the synthesized Co(II) complexes can be promising novel antimicrobial agents.

References

1. Nangia A, Desiraju GR (1999) Chem Commun 7:605-606

2. Thomas J, Ramanan A (2016) J Chem Sci 128:1687-1694

3. Elgrishi N, Chambers M B, Wang X, Fontecave M (2017) Chem Soc Rev 46:761-796

4. Wagenknechta P S, Ford P C (2011) Coord Chem Rev 255:591-616

5. Warra AA (2011) J Chem Pharm Res 3(4):951-958.

6. Haas KL, Franz KJ (2009) Chem Rev 109:4921-4960

7. Schwartz JA, Lium EK, Silverstein SJ (2001) J Virol 75:4117-4128

8. Chang EL, Simmers C, Knight DA (2010) Pharmaceuticals 3:1711-1728

9. Dimiza F, Papadopoulos AN, Tangoulis V, Psycharis V, Raptopoulou CP, Kessissoglou DP, Psomas G (2010) Dalton Trans 39:4517-4528

10. Dimiza F, Papadopoulos AN, Tangoulis V, Psycharis V, Raptopoulou CP, Kessissoglou DP, Psomas G J (2012) Inorg Biochem 107:54-64.

11. Patel M, Chhasatia M, Bhatt B (2011) Med Chem Res 20:220-230.

12. Sathyadevi P, Krishnamoorthy P, Alagesan M, Thanigaimani K, Thomas Muthiah P, Dharmaraj N (2012) Polyhedron 31:294-306

13. Ferreira SB, Kaiser CR (2012) Expert Opin Ther Pat 22:1033-1051

14. El-Emary T (2006) J Chin Chem Soc 53:391-401

15. Hamada M, Roy V, McBrayer TR, Whitaker T, Urbina-Blanco C, Nolan SP, Balzarini J, Snoeck R, Andrei G, Schinazi RF, Agrofoglio LA (2013) Eur J Med Chem 67:398-408

16. Hirshfeld FL (1977) Theoret Chim Acta 44:129-138

17. Spackman MA, Jayatilaka D (2009) Cryst Eng Comm 11:19-32

18. Spackman PR, Turner MJ, McKinnon JJ, Wolff SK, Grimwood DJ, Jayatilaka D, Spackman MA (2021) J Appl Cryst 54:1006-1011

19. R.A. Ayten (2019) Acta Crystallogr E75:1467-1471

20. Gumus I, Solmaz U, Binzet G, Keskin E, Arslan B, Arslan H (2018) J Mol Struct 1157:78-88

21. Chopra D (2018) Understanding intermolecular interactions in the solid state: Approaches and techniques (Vol. 26), Royal Society of Chemistry, UK

22. Spackman MA, McKinnon JJ, Jayatilaka D (2008) Cryst Eng Comm 10:377-388

23. Spackman MA, McKinnon JJ (2002) Cryst Eng Comm 4:378-392

24. Gavezzotti A (2002) J Phys Chem B 106 (16):4145-4154

25. Maloney AGP, Wood PA, Parsons S (2015) Cryst Eng Comm 17:9300-9310

26. Murray PR, Baron EJ, Pfaller MA, Tenover FC, Yolken HR (1995) Manual of Clinical Microbiology, 6th Ed. ASM Press, Washington DC

27. Meng XY, Zhang HX, Mezei M, Cui M (2011) Curr Comput Aided Drug Des 7(2):146-157

28. Morris GM, Huey R, Lindstrom W, Sanner MF, Belew KR, Goodsell DS, Olson AJ (2009) J Comput Chem 16:2785-2791

29. http://accelrys.com/products/discovery-studio/visualization-download.php

30. Morris GM, Goodsell DS, Halliday RS, Huey R, Hart WE, Belew KR, Olson AJ (1999) J Comput Chem 19:1639-1662

31. Rusbridge EK, Peng Y, Powell AK, Robinson D, Fitzpatrick AJ (2018) Dalton Trans 47:7644-7648

32. Kang W, Huo LH, Gao S, Ng SW (2009) Acta Crystallogr Sect E Struct Rep Online 65(12):m1502

33. Sang LT, Mukesh MJ, Edward RT (2019) Acta Crystallogr E75:308-318

34. Mackenzie CF, Spackman PR, Jayatilaka D, Spackman MA (2017) IUCr J 4(5):575-587

35. El-Megharbel SM, Adam AM, Meghdad AS, Refat MS (2015) Russ J Gen Chem 85:2366-2371
36. Patel MN, Pansuriya PB, Parmar PA, Gandhi DS (2008) Pharm Chem J 42:687-692
37. Sissi C, Palumbo M (2010) Cell Mol Life Sci 67:2001-2024